Catalysis Science & Technology

ROYAL SOCIETY OF CHEMISTRY

PAPER

Published on 22 October 2026
Licensed under CC-BY 4.0

Check for updates

Cite this: DOI: 10.1039/d6cy01323f

Hydrothermal stability of modified alumina-based catalyst supports under simulated high-conversion Fischer–Tropsch synthesis conditions

Sanele Moloi, [a] Anna Zimina, [b] Peter Nagel,[c] Genevéve Marx,[d] E. Jaco Olivier,[d] Thulani M. Nyathi, [a] Nico Fischer [a] and Michael Claeys *[a]

The chemical transformation of the widely utilized gamma-alumina (γ-Al_2O_3) catalyst support to form boehmite (γ-AlOOH) under hydrothermal conditions is unfavorable and can contribute to catalyst deactivation. For example, hydrothermal conditions are typically created in the Fischer–Tropsch synthesis (FTS) and can be detrimental to the performance of γ-Al_2O_3-supported FTS catalysts that need to operate at high carbon monoxide (CO) conversions. In this study, an unmodified γ-Al_2O_3 (Al) catalyst support was evaluated under various water partial pressures (P_{H_2O} = 2.0, 2.9, 5.3, 9.0, and 11.8 barg) in a total system pressure of 15.75 barg, simulating the hydrothermal environments realized at different CO conversions (X_{CO} = 30%, 40%, 60%, 80%, and 90%, respectively) in the FTS. Post-exposure to the highest water partial pressure (P_{H_2O} = 11.8 barg; X_{CO} = 90%), a decrease in the quantity of γ-AlOOH detected in the PXRD patterns of the spent modified Al supports was observed, when compared with unmodified Al. This decrease followed the order; Al (48.9 wt%) > MgAl (13.1 wt%) ≈ ZnAl (12.0 wt%) > SiAl (0.0 wt%). Despite challenges with quantification, the MnAl spent support contained γ-AlOOH and Mn_xO_y species after each test, with the presence of Mn_xO_y species indicating the exsolution of Mn from the MnAl support. Overall, the modification of Al improved the hydrothermal stability of the resultant supports by limiting γ-AlOOH formation under simulated high FTS-CO conversion conditions, with the stability level dependent on the type of dopant present in the support.

Received 14th September 2026,
Accepted 22nd October 2026

DOI: 10.1039/d6cy01323f

rsc.li/catalysis

1. Introduction

Catalyst supports are integral in the formulation and function of heterogeneous catalysts. Among other things, supports anchor catalyst nanoparticles and provide interactions that contribute to the overall function of a catalyst.[1–3] Alumina, specifically gamma-alumina (γ-Al_2O_3), is traditionally used in heterogeneous catalysis in a variety of applications.[2,4,5] These include the (reverse) water-gas shift, steam reforming of methane, carbon dioxide hydrogenation, and the Fischer–Tropsch synthesis (FTS).[6–8] A common feature of these reactions is the presence of water (H_2O) as either a reactant or product, which cannot be mechanistically omitted.

Water, be it in liquid or vapor phase, is known to contribute to the degradation of γ-Al_2O_3 and, subsequently, the loss of catalyst integrity and catalyst deactivation.[5,9,10] Although γ-Al_2O_3 is a very useful support with desirable characteristics, *e.g.*, high attrition resistance and thermal stability, water can induce chemical changes to the bulk structure of the γ-Al_2O_3 support at reaction temperatures above 150 °C.[5,10–13] This is reported to occur by means of a sequential mechanism where hydroxyl groups (–OH) precipitate (or the weathering of singly-coordinated surface Al–OH groups occurs) following the dissolution of bulk Al atoms.[5,10] For example, typical FTS conditions favor a hydrothermal environment because of the reaction temperature (*e.g.*, 220 °C) and the H_2O produced from the conversion of synthesis gas (*i.e.*, carbon monoxide (CO) and hydrogen (H_2), which also react to produce hydrocarbons).[11]

At an industrial level, particularly in slurry phase reactors, water can induce severe catalyst deactivation.[14] Under commercially relevant conditions (220–230 °C, 20–30 bar and 50–70% syngas conversions), where the catalysts must function for lengthy operation periods (*i.e.*, 2–3 years), the partial pressure of water ranges between 5 and 9 bar.[14–18] The catalyst passes through areas of high water partial pressures

[a] *Catalysis Institute, Department of Chemical Engineering, University of Cape Town, Rondebosch, Cape Town, 7700, South Africa. E-mail: michael.claeys@uct.ac.za*
[b] *Institute of Catalysis Research and Technology (IKFT), Karlsruhe Institute of Technology (KIT), Hermann-von-Helmholtz-Platz 1, 76344 Eggenstein-Leopoldshafen, Germany*
[c] *Institute for Quantum Materials and Technologies (IQMT) and Karlsruhe Nano and Micro Facility (KNMFi), Karlsruhe Institute of Technology, Kaiserstrasse 12, 76128 Karlsruhe, Germany*
[d] *Centre for High Resolution Transmission Electron Microscopy, Nelson Mandela University, South Campus, PO Box 7700, Gqeberha, 6031, South Africa*

because of extensive back-mixing and circulation.[14,15] Subsequently, the catalyst is permanently deactivated because of its interactions with water under FTS conditions. In the fixed-bed reactor configuration, catalysts experience severe deactivation (mostly) at the bottom of the catalyst bed where the partial pressure of water is highest.[14] In both reactor configurations, oxidation and the formation of stable metal–support compounds have been reported as the main deactivation mechanisms caused by interactions between water and the catalyst under FTS conditions.[14,17] Consequently, periodic catalyst rejuvenation and recycling steps are implemented to sustain FTS operation. This down time increases process costs and impedes productivity.[16,19] Thus, modifications to the catalysts (*i.e.*, modified supports and the use of promoters) have been employed to improve catalyst stability and overall function during the FTS.[20–22]

Hydrothermal conditions experienced during the FTS also contribute to catalyst deactivation by transforming γ-Al_2O_3 to boehmite (γ-AlOOH). Fischer *et al.*[12] observed needle-like structures in some sections of the TEM images of spent alumina-supported cobalt (Co) catalysts. These structures were linked to the transformation of parts of the parent alumina support to boehmite after exposure to FTS conditions. A study by Park *et al.*[23] reported that a partial transformation of the surface of γ-Al_2O_3 to form pseudo-boehmite surface species occurred during the FTS (CO conversions = 60–98.8%) over unpromoted and platinum (Pt)-promoted Co catalysts anchored on unmodified and phosphorous (P)-modified γ-Al_2O_3 supports. The catalysts supported on unmodified γ-Al_2O_3 experienced a faster rate of deactivation than those supported on P-modified γ-Al_2O_3. The basis of proposing the formation of pseudo-boehmite surface species was the presence of a deformation band assigned to physisorbed H_2O observed during *in situ* diffuse reflectance infrared Fourier transformation spectroscopy analysis.

Furthermore, the adsorbed H_2O contributed to the formation of an aggregated catalyst lump. A degree of aggregation, based on the catalyst lump, was calculated for the spent Co catalysts anchored on an unmodified γ-Al_2O_3 support as 8.7% for Co/γ-Al_2O_3 and 10.3% for Co/Pt/γ-Al_2O_3, respectively. No degree of aggregation was calculated for the Co/(P)-modified γ-Al_2O_3 and Co/Pt/(P)-modified γ-Al_2O_3 catalysts because a catalyst lump was not detected. A follow-up study by Park *et al.*[24] observed that after the FTS (CO conversions = 65–85%), distinct powder X-Ray diffraction (PXRD) reflexes – attributed to the boehmite phase – appeared in the PXRD patterns of spent Co catalysts anchored on unmodified and modified (with P, zinc (Zn) and zirconium (Zr), separately) γ-Al_2O_3 supports. The crystallite size (in nm) of the γ-AlOOH formed in each catalyst was linked to hydrothermal stability, with the least stable catalyst exhibiting the largest crystallite size of γ-AlOOH and the most stable catalyst exhibiting the smallest crystallite size of γ-AlOOH based on PXRD analysis of the spent catalyst samples. Therefore, the following increasing order in hydrothermal stability was established: Co/Zr/γ-Al_2O_3 (38.1 nm) < Co/Zn/γ-Al_2O_3 (35.4 nm) < Co/γ-Al_2O_3 (32.8 nm), with no γ-AlOOH detected in the spent Co/P/γ-Al_2O_3 catalyst, and the values in parentheses indicating the crystallite size of γ-AlOOH. Importantly, in both studies by Park *et al.*,[23,24] the transformation of γ-Al_2O_3 to γ-AlOOH was reported to contribute to the overall deactivation of the catalysts.

To circumvent this chemical transformation, there have been γ-Al_2O_3 modification methods proposed to offer stability against γ-AlOOH formation.[2,5] The study by Amrute *et al.*[5] reported the stabilization of alumina by transforming it to corundum (α-Al_2O_3) *via* thermal treatment. Subsequently, there was an improvement in the FTS performance and chemical stability of the Co/α-Al_2O_3 catalyst over 250 h time-on-stream (TOS). Though the study succeeded in this regard, the α-Al_2O_3 polymorph offered a lower surface area support because of its increased crystallinity (as evidenced *via* PXRD) after exposure of higher-surface-area γ-Al_2O_3 to a thermal treatment. Ravenelle *et al.*[25] reported that the presence of Ni (1 wt%) in Ni/γ-Al_2O_3 and Pt (1 wt%) in Pt/γ-Al_2O_3 significantly impeded γ-AlOOH formation during aqueous phase reforming conditions (which represent biomass reforming) by blocking specific surface hydroxyl groups and, subsequently, decreasing the rate of hydration to protect the support. Park *et al.*[23] reported that support modification with P decreased the hydrophilicity of the γ-Al_2O_3 support to yield lower sorption capacities of water in the microcavities. Thus, the catalysts anchored on the phosphorous-modified support demonstrated improved CO conversions and stability against γ-AlOOH formation during the FTS. Lastly, Abi Aad *et al.*[11] reported that the transformation of γ-Al_2O_3 to γ-AlOOH was inhibited through the doping of magnesium (Mg), Zr, Ni, and silicon (Si) into γ-Al_2O_3. This modification also improved the CO conversion of the final supported catalysts over 100 h in the FTS.

Herein, we explored stabilizing γ-Al_2O_3 against γ-AlOOH formation under hydrothermal conditions by individually doping small amounts ($\leq$5 wt%) of foreign elements, *viz.*, Mn, Mg, and Zn, into the γ-Al_2O_3 support. A commercial modified γ-Al_2O_3-based support containing small amounts of Si was also included in this study to enable a comparison with our synthesized modified supports. The conditions to which the supports were exposed (see section 2.3) are an experimental simulation of the hydrothermal environments created at different CO conversion levels during the FTS. However, it is important to note that these conditions may also apply to other reactions that involve H_2O as a reactant or product. It is also worth emphasizing that the study herein has taken a unique approach of investigating the hydrothermal stability of various γ-Al_2O_3-based supports in a fixed-bed reactor configuration, which allowed the flow of different amounts of water vapor (and argon) at a temperature (220 °C) and pressure (15.75 barg) that are close to those applied in realistic FTS. Further, because PXRD is sensitive to different crystallographic phases, it is the most

 This journal is © The Royal Society of Chemistry 2026

effective characterization technique for distinguishing and quantifying phases such as γ-Al_2O_3, γ-AlOOH, MAl_2O_4, and M_xO_y (where M = Mn, Mg, Zn, or Si) that may be present in the spent supports after hydrothermal stability testing. Collectively, these experimental approaches are paramount towards the design of chemically robust supports that can be used to prepare the next generation of highly active and stable FTS catalysts. The approach of using dopants to stabilize γ-Al_2O_3 is reported to be more attractive because the intrinsic physicochemical structure of the bulk support is not significantly altered. However, support properties such as surface acidity and basicity are altered to generally offer improved material performance during chemical reactions.[1,5,10,11] In essence, the modification of γ-Al_2O_3 is hypothesized to improve phase stability by inhibiting γ-AlOOH formation under various hydrothermal conditions that simulate different FTS conversion levels.

2. Methods

2.1. Catalyst supports synthesis

A series of modified γ-Al_2O_3-based supports, *viz.*, MnAl, MgAl, and ZnAl, were synthesized *via* incipient wetness impregnation. The targeted loading for each modifier was 5 wt%. In a typical synthesis, white γ-Al_2O_3 powder (SASOL Germany, PURALOX SCCa-5/150)[26,27] was used as the parent material to obtain the targeted supports. The precursor salts used were $Mn(NO_3)_2{\cdot}4H_2O$, $Mg(NO_3)_2{\cdot}6H_2O$, and $Zn(NO_3)_2{\cdot}6H_2O$ (all from Merck), respectively. To modify the parent γ-Al_2O_3 support, 2.50 g of salt was dissolved in *ca.* 10 mL of deionized water to produce a mixed salt solution. Note that the water–salt mixture used was equivalent to the pore volume of the unmodified γ-Al_2O_3 support. The mixture was deposited dropwise onto the γ-Al_2O_3 powder (20 g) using a disposable plastic Pasteur pipette. As the droplets were added, a grind-mixing action was used to mix the powder and droplets in a mortar using a pestle. A powder mixture was obtained in each case and then left to fully dry overnight in an oven that is preheated at 120 °C in static air. Once dried, the samples were ground into a fine powder using a pestle and mortar. The powders were then exposed to a heat treatment at 900 °C for 4 h (heating rate: 1.5 °C min^{-1}) in air (in the case of MgAl and ZnAl) or H_2 (in the case of MnAl) flowed at 68.4 mL min^{-1}. The MnAl support was exposed to a heat treatment of 900 °C in H_2 because other gas environments encouraged the presence of multiple oxide phases (*i.e.*, MnO and Mn_2O_3) in addition to the desired spinel oxide (*i.e.*, $MnAl_2O_4$). The appearance of the undesired oxides suggested that the Mn was not embedded into the Al support. Generally, this leaves the Al support vulnerable to phase transformation, hence, the presence of reflexes corresponding to α-Al_2O_3 in the diffraction patterns of the supports (see section 1 of the SI for the detailed synthesis method of MnAl). Thus, to limit the formation of phases other than the desired $MnAl_2O_4$, H_2 was used during the heat treatment of the MnAl support.

Essentially, a fine white powder was obtained for the MgAl and ZnAl supports, while the MnAl support exhibited a light brown colour. A commercial silica-modified alumina support with a Si loading of 2 wt% was obtained from SASOL Germany[26,27] and included as part of the series of modified supports to be used in this study. This silica-modified alumina support was used without any further purification or treatment. Thus, the series of supports to be evaluated under different hydrothermal conditions were unmodified alumina (*viz.*, Al) and modified alumina supports (*viz.*, MnAl, MgAl, SiAl, and ZnAl).

2.2. Characterization

2.2.1. Inductively coupled plasma-optical emission spectrometry (ICP-OES). The metal loading in each support was determined using ICP-OES. The samples (~0.05 g) were digested in a mixture of 8 mL *aqua regia* and 2 mL H_2SO_4. This was done using microwave radiation in a Mars 6 Microwave Digester over a heating period of 30 min from room temperature to 220 °C, with a hold time of 45 min at 220 °C. The digested samples were analysed in an Agilent 5800 ICP-OES instrument.

2.2.2. Nitrogen physisorption. Nitrogen (N_2) physisorption was conducted to determine the BET (Brunauer–Emmett–Teller) surface areas and BJH (Barrett–Joyner–Halenda) pore volumes and pore sizes of the fresh supports. A Micromeritics Tristar II 3020 instrument was used for the analyses. Prior to the N_2 physisorption and isotherm measurement, 0.05 g of each catalyst support was degassed under vacuum for 3 h at 200 °C. The mass-specific surface area of each sample was calculated (between a relative pressure range of 0.05 to 0.20) using the BET method.[28] The pore volumes were determined from the amount of N_2 gas adsorbed at a relative pressure of 0.99. Desorption isotherms were used to obtain the average pore volumes and pore sizes by applying the BJH method.[28]

2.2.3. X-ray Absorption Spectroscopy (XAS). XAS experiments were performed on the unmodified Al and modified Al-based support powders at the WERA beamline at KIT Light Source (Karlsruhe, Germany).[29] The X-ray absorption spectra, at the Al K-edge (1559.6 eV), were recorded at room temperature in fluorescence mode on the fresh supports and a commercial $MgAl_2O_4$ reference material. A small amount of powder was distributed over a thin layer of double-sided carbon tape. The thin layer is necessary to minimize self-absorption effects on the measurements as they are conducted in fluorescence mode. Thereafter, the samples were fixed on a metallic sample holder, which can be placed into the load-lock and evacuated.

2.2.4. Powder X-ray diffraction (PXRD). PXRD was carried out to determine whether the original bulk support structure was maintained, and most importantly, identify the small amounts of newly formed mixed-metal oxides (*viz.*, $MnAl_2O_4$, $MgAl_2O_4$, and $ZnAl_2O_4$) after incipient wetness impregnation. All recorded diffraction patterns were compared with the

diffraction lines of known (reference) mixed metal oxides from the ICDD PDF-4+ 2021 database. The PXRD pattern of each un-/modified support was recorded within the 2θ range of 20–120° using a Bruker D8 Advance X-ray diffractometer equipped with a Co source ($\lambda_{K\alpha1}$ = 0.178897 nm) operated at 35 kV and 40 mA and a position-sensitive LYNXEYE XE detector in Bragg–Brentano geometry. During the recording, a step size of 0.043° and a time per step of 0.75 s was used to achieve a total scan time of 29 min 50 s. Rietveld refinement was carried out on the obtained diffraction patterns of the fresh and spent support samples utilising the software package TOPAS 5.0 (Bruker AXS)[30] to determine the amount and crystallite size of boehmite (and other crystalline phases) present in each un-/modified support.

2.2.5. Raman spectroscopy. A BWTEK iRaman Prime spectrometer, equipped with a 532 nm (emitting green light) excitation laser operated at 35 mW power, was used to conduct Raman spectroscopy measurements. A sample probe was placed onto each fresh powder sample, and spectra were acquired. Each spectrum was acquired with an integration time of 5 s and averaged over 5 accumulations. A BWSPEC V4.15.10 software[31] was used to perform the acquisition and processing of data.

2.2.6. Ammonia temperature-programmed desorption (NH_3-TPD). NH_3-TPD experiments were performed in a Micromeritics AutoChem II 2920 chemisorption analyzer equipped with a thermal conductivity detector (TCD). Prior to the NH_3-TPD experiments, temperature-programmed reduction (in H_2) experiments were carried out for each sample. First, 110 mg of the support sample was loaded into a U-shaped quartz microreactor. The samples were purged to remove any residual water and volatile organic compounds present under Ar flow (50 mL (NTP) min^{-1}) at 150 °C (heating rate: 10 °C min^{-1}) for 1. The system temperature was decreased to 60 °C, the gas flow changed to 5% H_2/Ar at 50 mL (NTP) min^{-1}, and the temperature was increased to 925 °C at a heating rate of 10 °C min^{-1} for the reduction experiment. Recording of each reduction profile occurred concurrently with the temperature increase from 60 to 925 °C, and thereafter, the microreactor in the system was cooled to 100 °C under Ar flow (50 mL (NTP) min^{-1}) at 10 °C min^{-1}. After reduction, a gas change was conducted by switching to a 1% NH_3/He flow (50 mL (NTP) min^{-1}) for the commencement of the NH_3-TPD experiment. First, NH_3 was adsorbed onto the sample surface for 1 h at atmospheric pressure. This was followed by the desorption of weakly adsorbed NH_3 by purging in pure He (50 mL (NTP) min^{-1}) for 1 h at 100 °C. Afterwards, chemisorbed NH_3 was thermally desorbed by increasing the temperature to 850 °C at a heating rate of 10 °C min^{-1}. TCD signals were recorded during the NH_3 desorption process. Post analysis, the microreactor in the system was cooled to ambient temperature under Ar flow (50 mL (NTP) min^{-1}) at a rate of 10 °C min^{-1}.

2.2.7. Scanning Transmission Electron Microscopy (STEM). STEM analysis was carried out on the fresh supports and high-resolution STEM images were acquired with a double aberration corrected JEM-ARM200F transmission electron microscope operated at 200 kV (JEOL, Japan). The instrument has an advanced Gatan GIF 965ERS spectrometer fitted with dual Electron Energy Loss Spectroscopy (EELS) capabilities, as well as a XMax 100 TLE high collection angle and an ultra-sensitive energy-dispersive spectroscopy (EDS) detector (Oxford Instruments) for analysis by means of EELS and EDS. A sub-angstrom probe with a beam current ranging from 68 to 281 pA was used for the STEM analyses with a fixed probe convergence semi-angle of 23 mrad. The acceptance semi-angles were set to 84 mrad for the GIF, 34–137 mrad for the dark-field detector, and 0–12 mrad for the bright-field detector by using an illumination-limiting aperture. EELS spectrum imaging was performed over 2048 channels with a 1 eV channel width and a zero-loss peak FWHM of 1.5 eV. Elemental and compositional mapping were executed *via* model-based quantification routines (Hartree–Slater or Hydrogenic White Lines), excluding ELNES features. Lacey carbon sample grids (Agar Scientific) were used for HRSTEM purposes. STEM-EELS mapping of the supports (except for unmodified Al) was performed to identify and investigate Mn, Mg, Si, and Zn dopant distribution relative to the alumina support.

2.3. Hydrothermal stability testing (HST)

After characterization, the supports were exposed to various simulated FTS-CO conversion levels, *i.e.* X_{CO} = 30%, 40%, 60%, 80%, and 90%, respectively. Because the aim was to investigate the sole effect of H_2O, Ar was added as a balancing gas to represent the other reaction species (*i.e.*, unconverted syngas and formed FTS products) that would be present in a typical FTS environment at different conversion levels. The corresponding water partial pressures were: 2.0, 2.9, 5.3, 9.0, and 11.8 barg. A $\frac{1}{2}$ inch (*i.e.*, I.D.: 11.0 mm) fixed-bed reactor (length: 300 mm) was used for the support stability evaluation under hydrothermal conditions. Liquid water (see Table S1 for the respective flow rates) was fed into the system using a pre-calibrated HPLC pump (LabAlliance Series 1). The reactor line just before the fixed-bed rector was heated to 220 °C to enable the flash vaporisation of the water. This heated gas line was insulated to avoid H_2O condensation and pure Ar (20.0 mL min^{-1}) was flowed as a carrier for the H_2O vapor into the fixed-bed reactor. Furthermore, the reactor was heated at 220 °C under a pressure of 15.75 barg. The unmodified Al support (0.5 g) was exposed to the full P_{H_2O} range mentioned above, while the modified Al supports (0.5 g each) were exposed only to P_{H_2O} = 9.0 and 11.8 barg (representing X_{CO} = 80% and 90%, respectively). All supports were evaluated under the abovementioned water partial pressures for 3 h and the spent support samples were collected for PXRD analysis.

3. Results and discussions

3.1. Characterization and analysis

A series of surface and bulk techniques were used to determine the textural properties and composition of the

 This journal is © The Royal Society of Chemistry 2026

Table 1 Textural properties of the un-/modified catalyst supports

Catalyst support	$w_{element}$[a]/wt%	S_{BET}[b]/m^2 g^{-1}	P_{BET}[b]/cm^3 g^{-1}	P_{BET}[b]/nm	Sample colour
Unmodifed γ-Al_2O_3 (Al)	—	151	0.456	12.1	White
Mn-modified γ-Al_2O_3 (MnAl)	4.3 (5.0)	120	0.401	13.3	Pale brown
Mg-modified γ-Al_2O_3 (MgAl)	4.0 (5.0)	139	0.397	12.4	White
Si-modified γ-Al_2O_3 (SiAl)	2.3	142	0.460	12.9	White
Zn-modified γ-Al_2O_3 (ZnAl)	5.0 (5.0)	130	0.420	13.0	White

[a] Actual wt% loading determined by means of ICP-OES analysis and targeted wt% loading in parentheses. [b] Mass-specific surface areas, pore volumes and pore sizes obtained for the supports from N_2 physisorption measurements.

catalyst supports, with the relevant results summarised in Table 1. The sample naming convention and colour code scheme used herein to distinguish the catalyst supports are also shown. The elemental loadings of the modifiers (4–5 wt%) are close to the targeted 5 wt% loading. The commercial SiAl has a Si loading (2.3 wt%) that is approximately half that of the as-prepared modified supports. N_2 physisorption results show that modifying the parent Al support with Mn, Mg, and Zn decreases the mass specific surface area and pore volume below those of the unmodified Al support. This can be attributed to the high temperature treatment and the incorporation of the modifiers into the Al support structure. SiAl also exhibits a slightly lower surface area but still similar pore volume to that of the unmodified Al support. The similar pore sizes of all the supports indicate that the high temperature treatment (applied to obtain MnAl, MgAl, and ZnAl) did not alter the pore size of the parent Al support.

The supports all exhibit a white sample colour except MnAl (see Fig. S2). The colour exhibited is related to the type of cationic species of the dopant present on the surface or in the bulk of the Al-based support.[32] Si^{4+}, Zn^{2+}, and Mg^{2+} are reported to maintain the same valence state whether present inside or outside of the alumina matrix.[32–34] Hence, no colour change/s are exhibited by the Mg-, Si-, and Zn-modified Al supports. Mn exists in the 2+ or 3+ state when doped into the Al support. However, when present on the surface as a stand-alone oxide, the 3+ and 4+ states of Mn are also possible. Further, as the amount of Mn^{3+} doped into the Al support increases, a darker brown colour is exhibited.[32,35] Therefore, the pale brown colour observed is possibly a consequence of $Mn^{2+/3+}$ doping into the support, at the targeted low amounts. Note, some Mn_xO_y species may also be present on the surface to give the observed pale brown colour.

The diffraction patterns of the fresh supports, along with the relevant reference patterns (see Table S2 for data file descriptions), are shown in Fig. 1. The diffraction patterns of the modified Al supports are consistent with that of the unmodified Al support. However, a notable difference can be observed in the light-green-shaded region. This region can be used to identify potential spinel mixed metal oxide (MAl_2O_4; where M = modifier) formation as the reflexes of the modified supports (particularly MnAl, MgAl, and ZnAl) within the shaded region correspond to the diffraction lines of the relevant reference mixed metal oxide. Contrary to the observations made with the MgAl and ZnAl supports, the MnAl support does not show distinct reflexes in the region used to identify the presence of a MAl_2O_4 spinel phase. This suggests that the $MnAl_2O_4$ possibly present in the MnAl support may be below the detection limit of our XRD instrument in terms of the quantity and/or crystallite size of $MnAl_2O_4$. The lack of visible reflexes for stand-alone Mn, Mg, and Zn oxides possibly indicates that the dopants are completely embedded in the support as MAl_2O_4. If other oxides are present outside the Al matrix, these may also be in quantities (*i.e.*, weight loadings and/or crystallite sizes) that are below the detection limit of our PXRD instrument. The SiAl support shows no differences when compared with the unmodified Al. Further, the low loading and amorphous nature of silica (SiO_x) confine it to be below the detection limit of the PXRD instrument.[36]

Additionally, the crystallite sizes and quantities of the crystalline phases present in each support are shown in Table 2. The Al support showed 100 wt% alumina in its unmodified form and a crystallite size of 5.5 nm. The MgAl and ZnAl support samples show similar quantities (92.6 and 91.1 wt%, respectively) and crystallite sizes (9.1 and 8.3 nm, respectively) of the γ-Al_2O_3 phase. There were also no

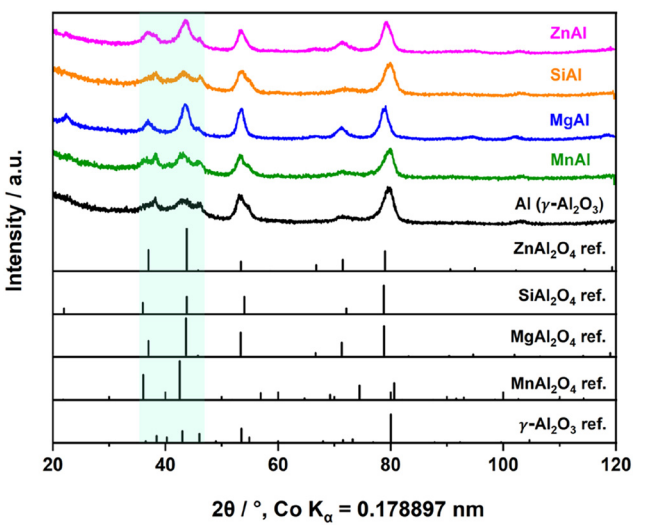


Fig. 1 PXRD patterns of the Mn-, Mg-, Si-, and Zn-modified γ-Al_2O_3 (MAl) supports and unmodified γ-Al_2O_3. Also shown are reference diffraction lines of the compounds that may be present in each support.

Table 2 Relative amounts and crystallite sizes of γ-Al_2O_3 and the relevant spinel phase determined *via* Rietveld refinement for the unmodified and modified Al support samples

Catalyst support	$W_{\gamma\text{-}Al_2O_3,XRD}$/wt%	$W_{MAl_2O_4,XRD}$/wt%	$Size_{Al_2O_3}$/nm	$Size_{MAl_2O_4}$/nm
Al	100	0.0	5.5 ± 0.1	—
MnAl	—	—	—	—
MgAl	92.6 ± 0.2	7.4 ± 0.2	9.1 ± 0.2	5.6 ± 0.1
SiAl	100.0	0.0	5.5 ± 0.1	—
ZnAl	91.1 ± 0.2	8.9 ± 0.2	8.3 ± 0.1	3.7 ± 0.1

significant differences observed when comparing the MAl_2O_4 phase quantities (7.4 and 8.9 wt%) and crystallite sizes (5.6 and 3.7 nm) of the MgAl and ZnAl supports, respectively. The SiAl support is modified with SiO_x, which is amorphous as no reflexes for Si-containing phases were observed. Therefore, the quantity (100 wt%) and crystallite size (5.5 nm) of the γ-Al_2O_3 phase in the SiAl support are comparable with those of the unmodified Al support. The increase in the crystallite size of the γ-Al_2O_3 phase (from 5.5–9.1/8.3 nm) when comparing the unmodified Al support with the MgAl and ZnAl supports is possibly a result of the high temperature treatment applied during the support synthesis (*i.e.*, calcination at 900 °C, see section 2.1). Owing to the absence of distinctly visible reflexes of $MnAl_2O_4$ in the PXRD pattern of MnAl, this phase could not be quantified using Rietveld refinement.

Furthermore, Fig. 2a and b show the Raman spectra of the fresh Al-based supports and the modifier-based oxides (*i.e.*, Zn-, Mg- and Mn-oxides), respectively. A baseline signal is observed in the spectrum of the Al support (Fig. 2a) because γ-Al_2O_3 is Raman inactive. The spectra of the modified Al supports also exhibit baseline signals. Furthermore, baseline signals are observed in the spectra of the Mn-based oxides (*viz.*, MnO, MnO_2 and Mn_2O_3) in Fig. 2b. This serves as evidence that the modified supports and the aforementioned Mn-oxide phases are also Raman inactive. Contrastingly, Mn_3O_4, MgO, and ZnO are Raman active because the spectra (Fig. 2b) of these oxides reveal distinct Raman bands. Noteworthy, the distinct Raman bands appearing in the spectra of Mn_3O_4, MgO, and ZnO do not appear in the spectra of the MnAl, MgAl, and ZnAl supports. Rather, baseline signals are exhibited in the spectra of all the modified Al supports. This proves that the modified supports have similar chemical bonding features to those of the unmodified Al support, and that no surface oxides (*e.g.*, Mn_3O_4, MgO and ZnO) are present on the modified Al supports. Thus, strengthening the case that the modifiers are doped into the Al support.

In essence, modified support materials with a predominantly bulk γ-Al_2O_3 structure and near-surface MAl_2O_4 compounds are proposed to have formed for the MnAl, MgAl and ZnAl, as a result of the synthesis method used herein.

To further investigate if the dopants are embedded in the Al-based supports as targeted, STEM-EELS analysis was carried out. Fig. 3 and 4 show the high-angle annular dark-field (HAADF), bright-field (BF), and STEM-EELS elemental maps of the MAl supports generated using the K and L-edges of the relevant constituent elements. The elemental maps recorded show intermetallic homogenous mixing between each dopant and the Al support constituent elements. This strengthens the case of each dopant being embedded within the Al support to form a modified near-surface layer constituting of a MAl_2O_4 phase.

It is worth mentioning that this may be a chemical mix, which produces the colour blends observed in the composite maps of the MnAl, MgAl, SiAl, and ZnAl samples (*i.e.*, blue + green = cyan). However, ZnAl seems to have some Zn species

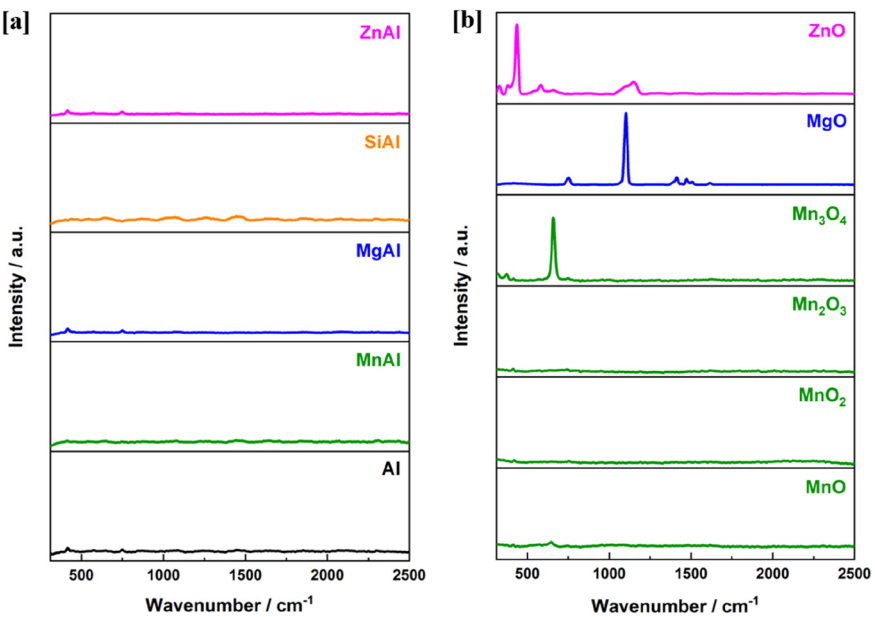


Fig. 2 Raman spectra of the (a) un/-modified Al catalyst supports and (b) the corresponding modifier-based oxides (excluding Si-based oxides).

This journal is © The Royal Society of Chemistry 2026

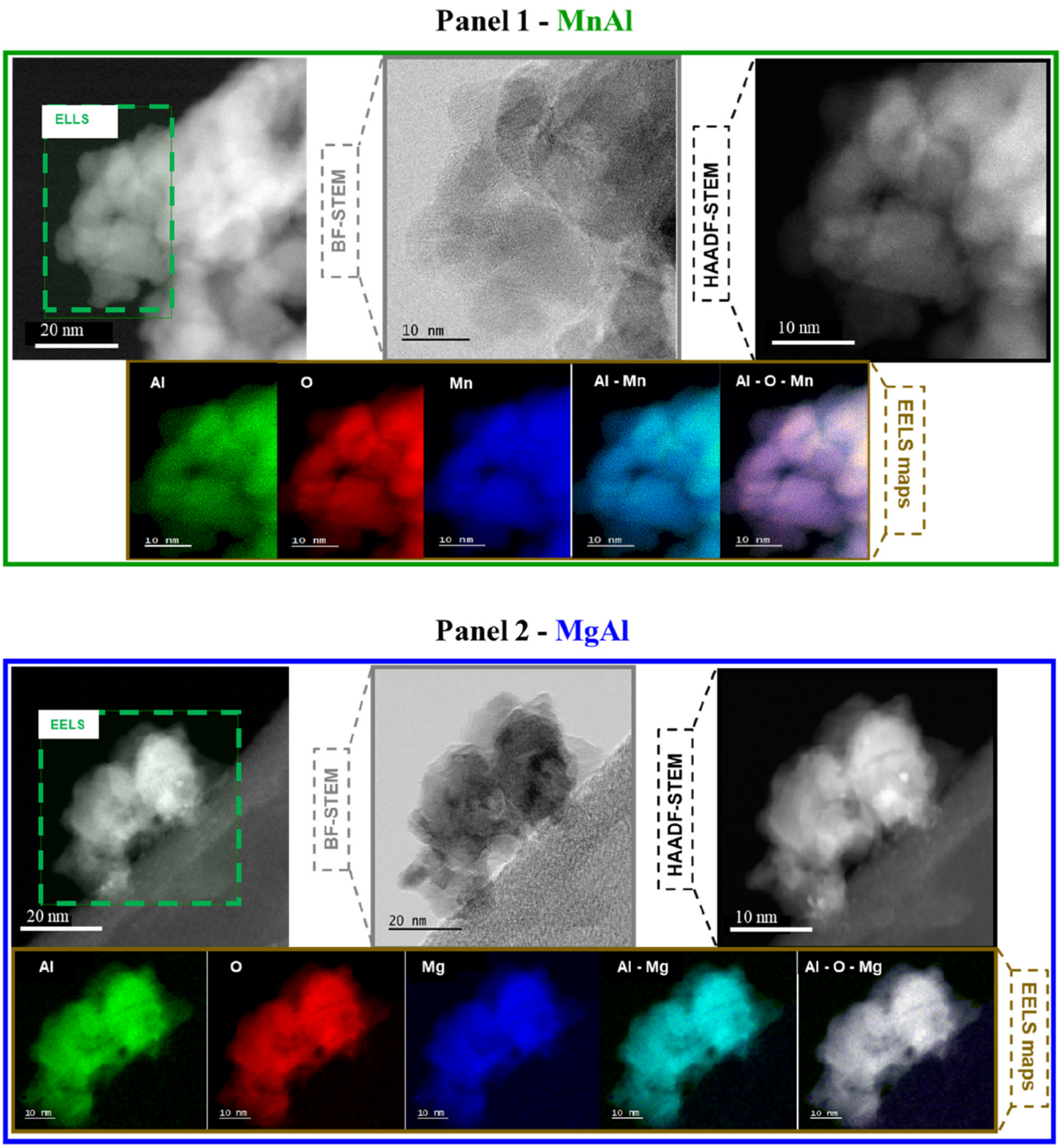


Fig. 3 (Top of all sample sets) Images captured in BF-STEM and HAADF-STEM modes. (Bottom of all sample sets) The STEM-EELS elemental maps showing the distribution of the constituent elements in the MnAl (panel 1) and MgAl (panel 2) supports.

that may not be embedded within the support matrix as evidenced by the appearance of a few small blue areas in the acquired composite maps (see the white dashed circles on the Al–Zn and Al–O–Zn composite maps in Fig. 4, panel 4). This can be further seen in the HAADF-STEM images where small nanoparticles contrast the ZnAl support. The position of these nanoparticles matches the small blue areas identified as Zn species in the EELS maps of the Al–Zn composite maps. Poor mixing and anchorage onto the Al support surface rather than into the pores of Al support during the synthesis may have resulted in the presence of these Zn-based nanoparticles.

Although not observed in the presented micrographs, the same may be true on some of the unimaged areas of the MnAl and MgAl samples. This may also occur because of the presence of excess dopant and/or incomplete reaction between the dopant and the parent Al support.

The supports were then characterized using XAS to study the local structure of aluminium in each support. Fig. 5 shows the Al K XANES spectra of the supports, and these are

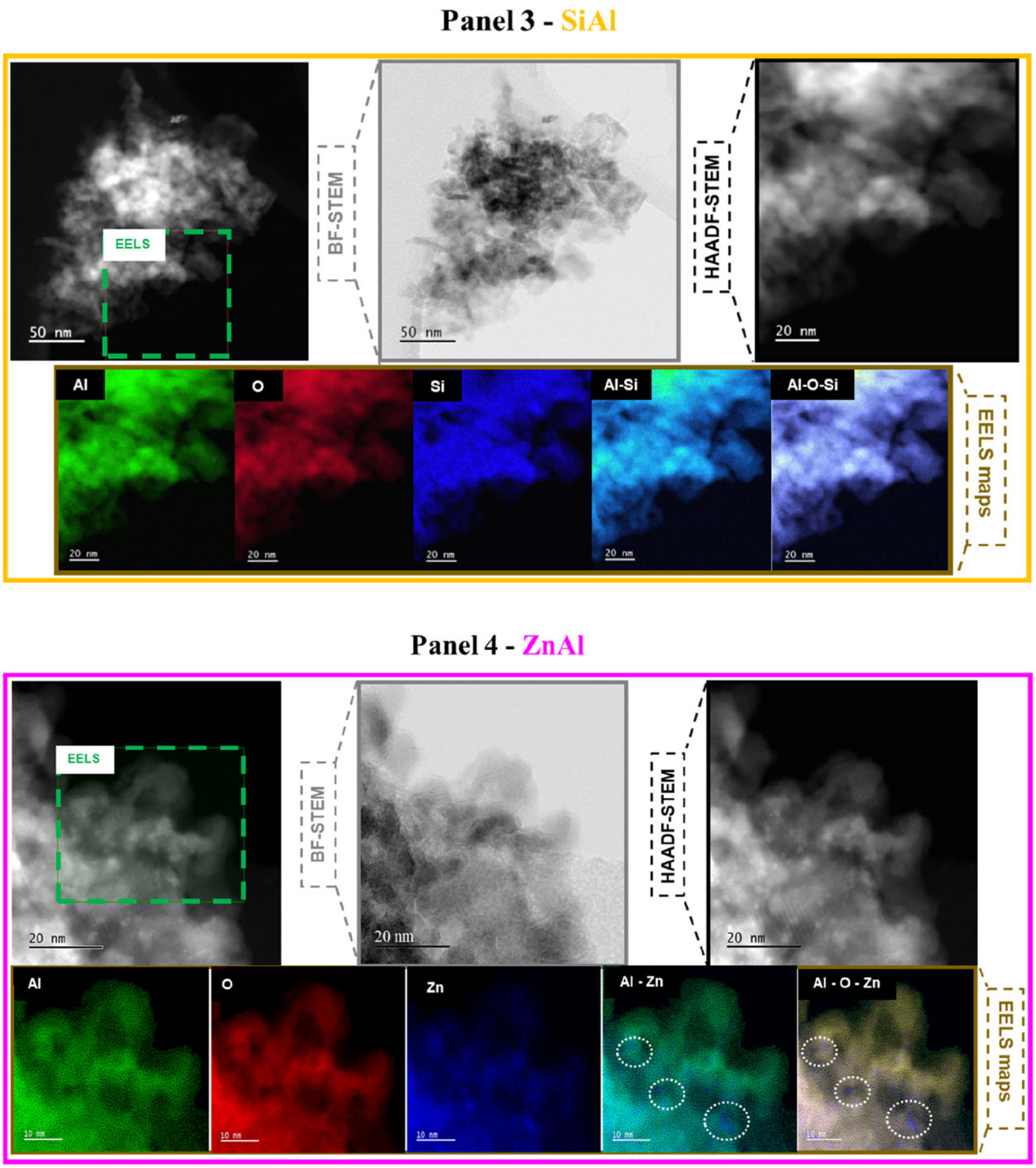


Fig. 4 (Top of all sample sets) Images captured in BF-STEM and HAADF-STEM modes. (Bottom of all sample sets) The STEM-EELS elemental maps showing the distribution of the constituent elements in the SiAl (panel 3) and ZnAl (panel 4) supports.

compared with a commercial spinel $MgAl_2O_4$ sample, which serves as a reference material for the characterisation.

The spectra of the MAl supports mirror that of the unmodified Al support and are superimposable, showing that there are no differences in the spectra of these samples. This suggests that the local structure of Al remains the same in each support. This finding is similar to that observed by Ildefonse *et al.* after comparing the Al K-edge XANES features of their Al-based materials.[37] Furthermore, using the rational reported by Westre *et al.*[38] (identified shifts between the Fe^{III} and Fe^{II} edges attributed to the change in the local geometry of the Fe atom due to the transition of valence electrons) and what can be extracted from XAS, it can be stated that the lack of obvious differences (such as spectral shifts) in the absorption spectra is a result of the aluminium exhibiting the same oxidation state and coordination geometry in all the

 This journal is © The Royal Society of Chemistry 2026

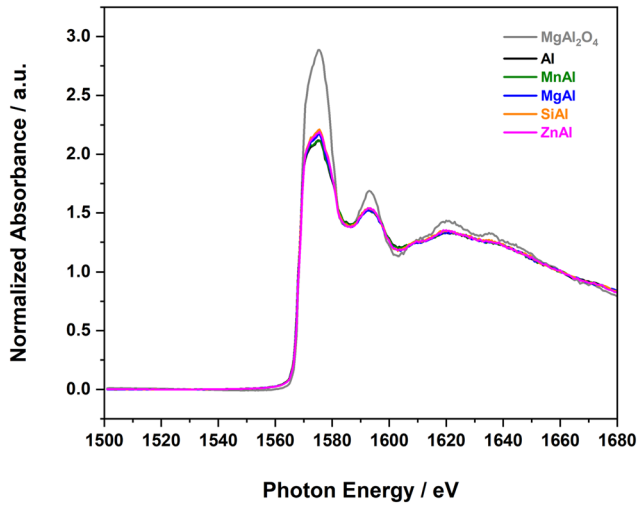


Fig. 5 A comparison of the normalized X-ray absorption spectra of the un-/modified alumina-based supports with the spectrum of the commercial $MgAl_2O_4$ reference material.

analysed supports. This excludes the commercial $MgAl_2O_4$ reference, which has different spectral features when compared with its close counterpart, MgAl, as well as the other Al-based supports. It is possible that the low loadings (≤5 wt%) of the dopants in each modified support are the reason for the lack of observable spectral shifts when comparing the collected spectra.[38]

In essence, our interpretation of the XAS results suggests that the Al-based supports have retained the characteristic features (or intrinsic structure) of the parent Al support, and that doping small amounts of a foreign element, as anticipated, does not significantly change the bulk support. This underpins the claim made from PXRD and HRSTEM-EELS analyses that support materials with a predominantly bulk γ-Al_2O_3 structure and a near-surface MAl_2O_4 layer are formed through doping.

The schematic in Fig. 6 shows our proposed evolution of the parent Al support to forming the MAl support through modification. a. The parent Al support with the sites responsible for metal (*i.e.*, modifier) consumption at the near-surface layers, b. the impregnation of the Al support with the modifier prior to the heat treatment stage, and c. the heat-treatment stage, where the powder mixture is heated to 900 °C and held for 4 h, which encourages the embedding of the dopant into the support sites responsible for metal consumption. During this stage, metal–support compounds (MSCs) form and modify the make-up of the near-surface layers of the support. This "pseudo" γ-Al_2O_3 near-surface may potentially exhibit slight differences in its properties (*e.g.*, acid–base and/or electronic). For instance, when comparing the NH_3-TPD profiles (see Fig. S2) of the un/-modified Al supports, there are differences in the desorption peak positions. The unmodified Al support shows a low- (137 °C) and a high-temperature (220 °C) desorption peak assigned to weak and strong acidic sites, respectively. The same desorption peaks for the modified supports appear within 94–104 °C and 206–212 °C, respectively. The desorption peak shifts provide evidence of the differences in the surface acidic strength of the un/-modified Al supports; a testament to the effect modification has on the surface properties of the Al support.

Because of this, or any other possible alternations, the Al support is deemed "modified" and no longer the same as the original Al support at the near-surface. Fu *et al.*[32] reported that doping may occur at the surface or through the material (into the bulk) depending on the synthesis method. Therefore, it is worth acknowledging that the method of

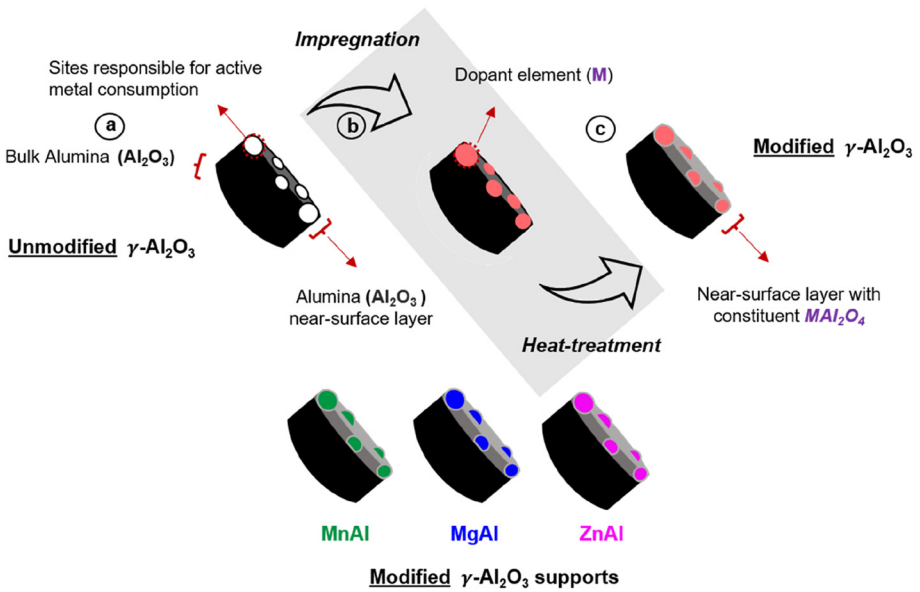


Fig. 6 A schematic representation of the proposed evolution of the unmodified Al support (a) to a modified Al support after (b) impregnation (highlighted with a light grey box) at an elevated temperature (c).

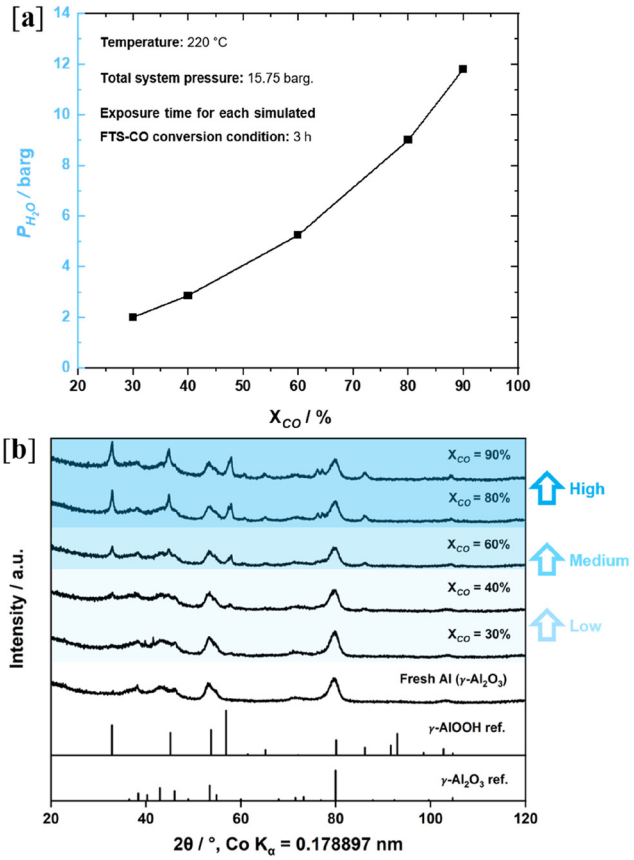


Fig. 7 [a] P_{H_2O} simulating the relative quantity of vaporized water that would be present at different CO conversion levels during the FTS. [b] PXRD showing the changes in the chemical and crystalline phase composition of the Al support under the different simulated FTS-CO conversion conditions.

doping used herein may also result in some of the dopants being embedded deep into the bulk of the support. Nonetheless, the Al support has been modified to satisfaction *via* the synthesis method employed in our current study.

3.2. Hydrothermal stability tests (by simulating different CO conversion levels realised in the FTS)

The unmodified Al support was exposed to different water partial pressures, *i.e.*, P_{H_2O} = 2.0, 2.9, 5.3, 9.0, and 11.8 barg, corresponding to X_{CO} = 30%, 40%, 60%, 80%, and 90%, respectively, at 220 °C and 15.75 barg. Fig. 7a shows the general relationship between water partial pressure and CO conversion in the FTS. As mentioned in section 2.3, Ar was added as a balancing gas that helps represent the other reaction species (*i.e.*, unconverted syngas and formed FTS products) that would be present in a typical FTS environment at different conversion levels. The temperature of 220 °C and pressure of 15.75 barg were chosen because they are close to the temperature and pressure applied in industrial FTS when using Co-based catalysts.[39,40] The chosen pressure also lies well below the vapour pressure of H_2O, which is 22.2 barg at 220 °C.[41] Fig. 7b shows the acquired PXRD patterns of the spent unmodified Al support samples after exposure to different water partial pressures that simulate FTS-CO conversion levels ranging from 30 to 90%. Table 3 presents a summary of the amounts and crystallite sizes of the γ-AlOOH detected by PXRD and quantified by means of Rietveld refinement for the unmodified Al support samples exposed to incremental water partial pressures at 220 °C and 15.75 barg. Table S3 provides the quantities and crystallite sizes of the γ-Al_2O_3 remaining after exposure to the abovementioned conditions.

Table 3 Relative amounts and crystallite sizes of γ-AlOOH determined *via* Rietveld refinement for the unmodified Al support samples after exposure to incremental water partial pressures (*i.e.*, incremental simulated FTS-CO conversion conditions) at 220 °C and 15.75 barg

Catalyst support	P_{H_2O}/barg	$X_{CO_{simulated}}$/%	$W_{AlOOH,XRD}$/wt%	$Size_{AlOOH}$/nm
γ-Al_2O_3	2.0	30	0.0	0.0
	2.9	40	6.01 ± 0.8	17.9 ± 3.6
	5.3	60	15.3 ± 0.7	19.0 ± 1.5
	9.0	80	25.4 ± 0.7	20.5 ± 1.0
	11.8	90	48.9 ± 0.8	19.2 ± 0.5

After 3 h of hydrothermal stability testing (HST) of the unmodified Al support at a simulated 30% FTS-CO conversion condition, there are no observable changes in the acquired PXRD pattern when compared with the acquired PXRD pattern of the fresh unmodified Al support (see Fig. 7b). Also, based on Rietveld refinement of the diffractogram of the spent Al support, there is 0 wt% γ-AlOOH present. After a simulated FTS-CO conversion of 40%, less intense reflexes at 33°, 58°, and 86.5° 2θ are observed. These reflexes are characteristic of γ-AlOOH, with the estimated relative amount of this phase being 6.01 wt% (see Table 3) and corresponds to a 17.9 nm crystallite size. However, the bulk of the Al support still composes of the γ-Al_2O_3 phase. When the simulated FTS-CO conversion is increased to 60%, the intensity of the γ-AlOOH reflexes at 33°, 58°, and 86.5° 2θ increase, with a new reflex at 45° 2θ also appearing. This condition produced an estimated amount of 15.3 wt% of γ-AlOOH, with a slight growth in the crystallite size to 19.0 nm, demonstrating a more apparent loss in the hydrothermal stability of γ-Al_2O_3. This effect becomes exacerbated when the Al support is exposed to higher simulated FTS-CO conversion conditions of 80% and 90%, where the relative amounts of γ-AlOOH present in the corresponding spent samples are 25.4 and 48.9 wt%, respectively. Although there is no significant change in the crystallite sizes, these high estimated amounts of γ-AlOOH are justified by the observed highly intense γ-AlOOH reflexes that start to overwhelm the reflexes of γ-Al_2O_3. The increase in the quantity of γ-AlOOH detected after exposure to HST at simulated FTS-CO conversions from 30–90% concomitantly led to a decrease in the γ-Al_2O_3 phase quantity detected (100–51.1 wt%), with no significant changes observed in the crystallite size (~6.5 nm) of the same phase (see Table S3).

This journal is © The Royal Society of Chemistry 2026

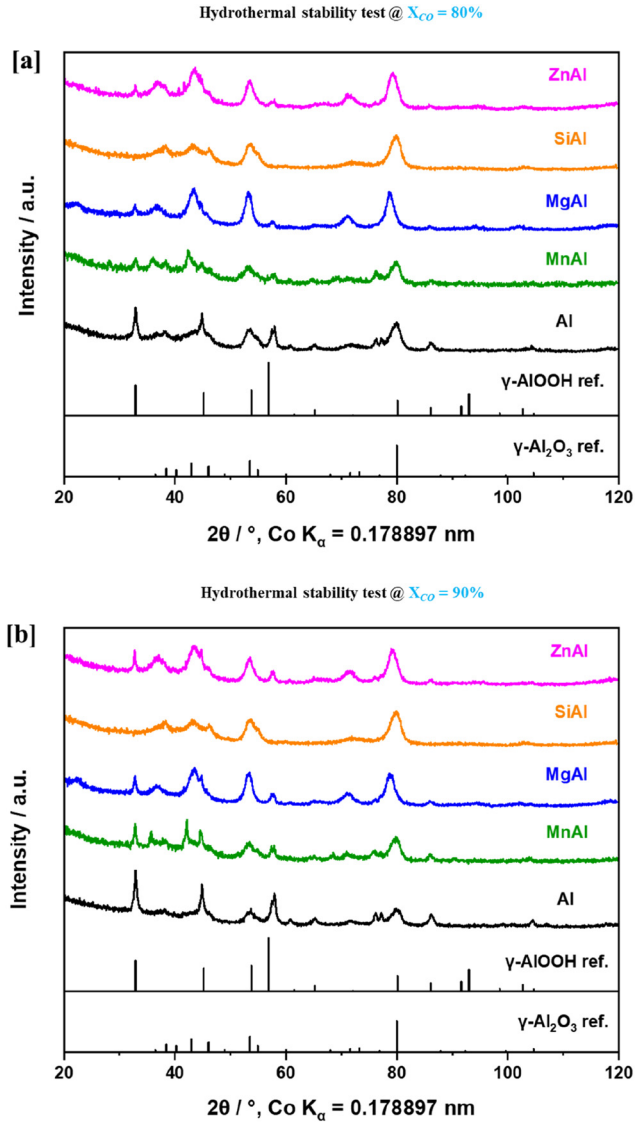


Fig. 8 A comparison of the chemical and crystalline phase changes of the un-/modified Al supports (based on PXRD analysis) after exposure to simulated [a] 80% and [b] 90% FTS-CO conversion conditions.

The modified Al supports were then exposed to two water partial pressure conditions, *i.e.*, P_{H_2O} = 9.0 and 11.8 barg, corresponding to X_{CO} = 80% and 90%, respectively, also at 220 °C and 15.75 barg. These conditions were chosen because this is where the unmodified Al support experienced the most considerable loss in hydrothermal stability. Fig. 8 shows the acquired PXRD patterns of the spent modified Al supports after exposure to the above-mentioned conditions. Table 4 provides a summary of the relative amounts and crystallite sizes of γ-AlOOH detected by PXRD and quantified by means of Rietveld refinement for the same spent supports. The quantities and crystallite sizes of the γ-Al_2O_3 and MAl_2O_4 remaining after exposure to the abovementioned conditions are given in Tables S4 and S5, respectively.

After 3 h of HST of the modified Al support samples at a simulated FTS-CO conversion of 80%, there are observable changes in the acquired PXRD patterns (see Fig. 8a). The reflexes at 33°, 45° and 58° 2θ, which are characteristic of γ-AlOOH, are observed for the ZnAl, MgAl, and MnAl spent supports. These reflexes have a lower intensity when compared with those of the predominant γ-Al_2O_3 phase. The estimated amount of γ-AlOOH in the spent MgAl and ZnAl supports is 6.8 and 7.1 wt% (see Table 4), respectively. All the other detected phases (*viz.*, γ-Al_2O_3 and MAl_2O_4) account for 93.2 and 92.9 wt% (see Table S4), respectively, of the recovered spent samples. Furthermore, similar crystallite sizes of the detected γ-Al_2O_3 (8.8 and 8.4 nm) and MAl_2O_4 (4.2 and 3.6 nm) phases were observed in the MgAl and ZnAl supports, respectively. Therefore, the MgAl and ZnAl supports exhibited minimal phase change when compared with the unmodified Al support after exposure to a simulated FTS-CO conversion of 80% (see Table 4). The MnAl support experiences the most significant change as can be observed in the acquired PXRD pattern. Besides the observed γ-AlOOH reflexes, other reflexes (within the 2θ region of 35–50°), possibly characteristic of multiple Mn_xO_y phases, can also be observed. These Mn_xO_y phases can only form if Mn exsolution or segregation out of the Al matrix occurred, suggesting that exposure to a relatively high water partial pressure may have caused the exsolution of Mn from the Al support. Unfortunately, the appearance of multiple Mn_xO_y phases presented challenges when attempting to quantify the formed amount of γ-AlOOH. This was due to extensive reflex overlaps owing to the presence of many crystalline phases in the spent sample (*viz.*, Al_2O_3, γ-AlOOH, $MnAl_2O_4$, and Mn_xO_y). This made it difficult to accurately

Table 4 Relative amounts and crystallite sizes (the latter is in parentheses) of γ-AlOOH determined *via* Rietveld refinement for the Al-based support samples after exposure to water partial pressures corresponding to simulated FTS-CO conversions of 80% and 90% at 220 °C and 15.75 barg

	$W_{AlOOH,XRD}$/wt% ($Size_{AlOOH}$/nm)	
Catalyst support	P_{H_2O} = 9.0 barg (X_{CO} = 80%)	P_{H_2O} = 11.8 barg (X_{CO} = 90%)
Al	25.4 ± 0.7 (20.5 ± 1.0)	48.9 ± 0.8 (19.2 ± 0.5)
MnAl	—[a]	—[a]
MgAl	6.8 ± 0.5 (23.8 ± 2.9)	13.1 ± 0.5 (21.0 ± 1.4)
SiAl	0.0	0.0
ZnAl	7.1 ± 0.5 (19.2 ± 2.2)	12.0 ± 0.4 (26.6 ± 1.7)

[a] Different Mn_xO_y phases possibly exist on the surface of the support, making the quantification of boehmite (by means of Rietveld refinement in TOPAS 5.0) inaccurate and otherwise misleading. Thus, no values are presented in the table.

and reliably deconvolute the contributions of each crystallographic phase (using Rietveld refinement) to the acquired PXRD pattern.

There are no observable reflexes corresponding to γ-AlOOH in the diffraction pattern of the spent SiAl support. Instead, the fresh and spent SiAl support exhibit the same PXRD patterns. It is worth mentioning that an inverse relationship exists between the amount of boehmite detected after HST and the hydrothermal stability of a support. In other words, a high relative amount of boehmite detected in the spent support indicates a low hydrothermal stability for that support, while a low relative amount of boehmite detected indicates high hydrothermal stability. Therefore, the hydrothermal stability of the supports after exposure to a simulated FTS-CO conversion of 80% increases in the following order: Al (25.4 wt%) < ZnAl (7.1 wt%) ≈ MgAl (6.8 wt%) < SiAl (0 wt%), with the value in parentheses indicating the amount of boehmite detected in the corresponding spent support.

The same changes observed in the acquired PXRD patterns after exposure to a simulated FTS-CO conversion of 80% (see Fig. 8a) can also be observed in the acquired PXRD patterns recorded post-exposure to 3 h of HST at a simulated FTS-CO conversion of 90% (see Fig. 8b). However, a significant increase in the intensity of the γ-AlOOH reflexes at 33°, 45°, and 58° 2θ is observed in the diffraction patterns of the spent ZnAl, MgAl, and MnAl supports. The estimated amount of γ-AlOOH is 13.1 and 12.0 wt% (see Table 4) in the spent MgAl and ZnAl supports, respectively, indicating a 1.9-fold (MgAl) and 1.7-fold (ZnAl) increase in the γ-AlOOH content when compared with the amounts estimated after a simulated FTS-CO conversion of 80%. It is worth mentioning that the crystallite sizes of the γ-Al_2O_3 and MAl_2O_4 phases reported for the fresh (see Table 2) and spent (see Tables S4 and S5) MgAl and ZnAl supports, after exposure to the two simulated conversion levels, are similar. However, there is a decrease in the relative weights of these phases when comparing the fresh and spent MgAl and ZnAl supports. This change is due to the phase transformation from γ-Al_2O_3 to γ-AlOOH which occurred during exposure to hydrothermal conditions at high water partial pressures (P_{H_2O} = 9.0 and 11.8 barg). There was also no change in the crystallite size (23.8 and 21.0 nm) of γ-AlOOH detected in the MgAl support sample after exposure to the two simulated conversion levels. The only notable difference in the crystallite size (19.2 nm at 80% and 26.6 nm at 90% FTS-CO conversion) of the γ-AlOOH phase was exhibited by the ZnAl support after exposure to the two simulated conversion levels. Thus, an increase in P_{H_2O} from 9.0 to 11.8 barg (*i.e.*, increasing the simulated X_{CO} from 80% to 90%) results in a decrease in the hydrothermal stability of the MgAl and ZnAl supports based on the observed increase in the relative amount of γ-AlOOH formed.

Similarly, an increase in the intensity of the reflexes within the 2θ region of 35–50° in the PXRD pattern of the spent MnAl support is observed, suggesting possible further exsolution of Mn from the Al matrix. Again, there are no observable reflexes corresponding to γ-AlOOH in the diffraction pattern of the spent SiAl support. As in the previous case (*i.e.*, a simulation of a FTS-CO conversion of 80%), an inverse relationship between the amount of boehmite detected in the spent support and the hydrothermal stability of the support is also apparent in this case (*i.e.*, after a simulation of a FTS-CO conversion of 90%). Therefore, the hydrothermal stability of the supports after exposure to a simulated FTS-CO conversion of 90% increases in the following order: Al (48.9 wt%) < MgAl (13.1 wt%) ≈ ZnAl (12.0 wt%) < SiAl (0 wt%), again, with the value in parentheses indicating the amount of boehmite detected in the corresponding spent support.

When exposed to simulated 80% and 90% CO conversion conditions, the modified supports generally showed improved hydrothermal stability than the unmodified γ-Al_2O_3. The hydrothermal stability order established is as follows: Al < MnAl < MgAl ≈ ZnAl < SiAl, with the Al support demonstrating the least hydrothermal stability and the SiAl support demonstrating the highest hydrothermal stability. Al modification by Si is reported to form surface Si–O–Al and Si–O–Si bonds, which are resistant to cleavage by water (or water adsorption).[11,36] In addition, these surface bonds are covalent and poorly soluble in water.[11] Therefore, the dissolution and/or reaction of γ-Al_2O_3 in/with water is prevented. Surface bonds of this nature (M–O–Al) are also thought to exist on the MgAl, ZnAl, and MnAl supports after the incorporation of the corresponding dopant into the Al support. Based on the hydrothermal stability trend established above, the cleavage resistance appears to be dopant dependent and decreases from the SiAl to the MnAl support. Note that in the case of the MnAl support, the exsolution of Mn from the Al support is proposed. This not only formed multiple Mn_xO_y phases but also exposed the singly coordinated Al–OH sites on the support that encourage γ-AlOOH formation. Mn^{2+} exsolution has been reported to occur in water from a diffusion layer of an electrolytic manganese residue to the bulk solution,[42] with the extent of exsolution increasing with an increase in temperature and water amount. Although this study pertains to the extraction of metals from solid mineral ore waste, it gives an account of the effect of temperature and water amount towards Mn exsolution. Thus, the exsolution of Mn from the Al support (in our study) could potentially be encouraged by the hydrothermal conditions applied, particularly the high water partial pressures simulating a FTS-CO conversion of 80% and 90%. More specifically, the bonds between the manganese and aluminium (in the form Mn–O–Al) may be easily weakened and broken under hydrothermal conditions to facilitate the exsolution of Mn. In the case of unmodified Al, the singly coordinated Al–OH sites are exposed and easily accessible to react with water.[10,11] Further, the formation of γ-AlOOH from the reaction of H_2O and γ-Al_2O_3 is kinetically favored at high water partial pressures and reaction temperature.[43–45]

 This journal is © The Royal Society of Chemistry 2026

Boehmite formation is reported to also occur through the involvement of the defect sites on γ-Al_2O_3, which are the so-called "weak spots" of the support as they easily adsorb and react with water.[4,5,10] Therefore, it can also be hypothesized that the modified supports (particularly SiAl, ZnAl, and MgAl) have fewer γ-Al_2O_3 defect sites or "weak spots". More specifically, these modifiers may have formed new chemical bonds with the parent support through the defect sites such that the reaction of water with the resultant support surface becomes inhibited. Thus, the chemical transformation to γ-AlOOH becomes increasingly harder or hindered even under mild-to-harsh hydrothermal conditions (or medium-to-high CO conversions in the FTS).

Thus, instead of transforming bulk γ-Al_2O_3 to the bulk α-Al_2O_3 phase (with a lower surface area and no defects), as done by Amrute *et al.*,[5] chemical modification of the support (through doping) is an attractive alternative towards stabilizing γ-Al_2O_3 against γ-AlOOH formation under hydrothermal conditions. This is because the same overall stabilization effect is achieved without a significant loss of the intrinsic bulk physicochemical characteristics of the γ-Al_2O_3 support.

4. Summary and conclusions

Water is innate to and cannot be avoided in some critical chemical reactions such as the FTS. The presence of water renders hydrothermal conditions part and parcel of the FTS. These conditions favor the transformation of γ-Al_2O_3 to γ-AlOOH, thereby destabilizing the catalyst support and hindering its optimal functioning. This is undesirable, especially in cases where the performance of a γ-Al_2O_3-supported catalyst is critical to ensuring an optimal chemical reaction. To circumvent this, a minor chemical modification of a γ-Al_2O_3 support (rather than applying thermal treatment only) was carried out by separately doping foreign elements (*viz.*, Mn, Mg, Si, and Zn) into γ-Al_2O_3. Through doping, modified supports that preserved the bulk physicochemical characteristics of the parent γ-Al_2O_3 support were produced. After exposure to various hydrothermal conditions, which simulated the hydrothermal environments realized at different CO conversion levels during the FTS, the unmodified Al support experienced significant transformation to γ-AlOOH. After exposure to high simulated FTS-CO conversion conditions, the MnAl support also experienced significant transformation to γ-AlOOH, demonstrating that the Al support modification approach explored with Mn does not improve the hydrothermal stability of the resultant support. Further, exsolution of the Mn out of the Al support to form a mixture of stand-alone Mn_xO_y phases is believed to have occurred. The exsolution is proposed to be caused by the high water partial pressures applied, which facilitated the weakening and consequent cleavage of the Mn–O–Al bonds.

However, modifying the Al support with Mg, Si, and Zn improved the hydrothermal stability of the resultant supports under high simulated FTS-CO conversion conditions, with SiAl being the most stable. These modifiers limited/inhibited γ-AlOOH formation within the γ-Al_2O_3 support and did not leach out of the support to form stand-alone metal oxides. We propose that the dopants (partially) block the defect sites of the support that would otherwise react with water to form γ-AlOOH at elevated reaction temperatures and pressures. Further, these supports possibly form hard-to-cleave M–O–Al bonds that are poorly soluble and inhibit water adsorption to form γ-AlOOH. The experimental approach taken in this study and the results obtained thereof are the first of their kind. Moreover, the experimental approach provides a meaningful simulation of realistic FTS conditions and our findings pave the way for the exploration of modified γ-Al_2O_3 supports in other chemical reactions that involve mild-to-harsh hydrothermal conditions.

Author contributions

All authors have contributed to the writing of the manuscript. The authors have all given approval of the final version of the manuscript.

Conflicts of interest

There are no conflicts to declare.

Data availability

Supplementary information: manganese-modified Al_2O_3 support synthesis, powder X-ray diffraction (PXRD) characterization, gaseous and liquid flow rate data corresponding to simulated CO conversions and water partial pressures, catalyst powder sample colors, NH_3-TPD of the Al-based supports, PXRD reference data files, Rietveld refinement fitting for phase quantity and crystallite size results. See DOI: https://doi.org/10.1039/d6cy01323f.

Acknowledgements

The authors would like to gratefully acknowledge the financial support from the Catalysis Institute, National Research Foundation, Department of Science, Technology and Innovation, as well as the South African National Energy Development Institute, as part of the CoalCO_2-X flagship programme. Furthermore, we extend our gratitude to Mr. Mufudzi Chaza for assisting with carrying out some of the hydrothermal experiments and Dr. Timothy Underwood for carrying out the Raman characterization of the materials. We are grateful to the KIT Light Source (Karlsruhe, Germany) for the provision of beamtime.

References

1 R. Munirathinam, D. Pham Minh and A. Nzihou, Effect of the Support and Its Surface Modifications in Cobalt-Based

Fischer–Tropsch Synthesis, *Ind. Eng. Chem. Res.*, 2018, **57**(48), 16137–16161, DOI: 10.1021/acs.iecr.8b03850.
2 G. Busca, The surface of transitional aluminas: A critical review, *Catal. Today*, 2014, **226**, 2–13, DOI: 10.1016/j.cattod.2013.08.003.
3 C. Mager-Maury, C. Chizallet, P. Sautet and P. Raybaud, Platinum Nanoclusters Stabilized on γ-Alumina by Chlorine Used As a Capping Surface Ligand: A Density Functional Theory Study, *ACS Catal.*, 2012, **2**(7), 1346–1357, DOI: 10.1021/cs300178y.
4 M. A. Sakwa-Novak and C. W. Jones, Steam Induced Structural Changes of a Poly(ethylenimine) Impregnated γ-Alumina Sorbent for CO2 Extraction from Ambient Air, *ACS Appl. Mater. Interfaces*, 2014, **6**(12), 9245–9255, DOI: 10.1021/am501500q.
5 A. P. Amrute, K. Jeske, Z. Łodziana, G. Prieto and F. Schüth, Hydrothermal stability of high-surface-area α-Al2O3 and its use as a support for hydrothermally stable fischer–tropsch synthesis catalysts, *Chem. Mater.*, 2020, **32**(10), 4369–4374.
6 C. Panzone, R. Philippe, A. Chappaz, P. Fongarland and A. Bengaouer, Power-to-Liquid catalytic CO2 valorization into fuels and chemicals: focus on the Fischer-Tropsch route, *J. CO2 Util.*, 2020, **38**, 314–347, DOI: 10.1016/j.jcou.2020.02.009.
7 W. Marquart, S. Raseale, G. Prieto, A. Zimina, B. B. Sarma, J.-D. Grunwaldt, M. Claeys and N. Fischer, CO2 Reduction over Mo2C-Based Catalysts, *ACS Catal.*, 2021, **11**(3), 1624–1639, DOI: 10.1021/acscatal.0c05019.
8 S. Raseale, W. Marquart, K. Jeske, G. Prieto, M. Claeys and N. Fischer, Supported Fe_xNi_y catalysts for the co-activation of CO_2 and small alkanes, *Faraday Discuss.*, 2021, **229**, 208–231, DOI: 10.1039/c9fd00130a.
9 N. Duyckaerts, M. Bartsch, I.-T. Trotuş, N. Pfänder, A. Lorke, F. Schüth and G. Prieto, Intermediate Product Regulation in Tandem Solid Catalysts with Multimodal Porosity for High-Yield Synthetic Fuel Production, *Angew. Chem., Int. Ed.*, 2017, **56**(38), 11480–11484, DOI: 10.1002/anie.201705714.
10 R. Réocreux, É. Girel, P. Clabaut, A. Tuel, M. Besson, A. Chaumonnot, A. Cabiac, P. Sautet and C. Michel, Reactivity of shape-controlled crystals and metadynamics simulations locate the weak spots of alumina in water, *Nat. Commun.*, 2019, **10**(1), 3139, DOI: 10.1038/s41467-019-10981-9.
11 J. Abi Aad, P. Courty, D. Decottignies, M. Michau, F. Diehl, X. Carrier and E. Marceau, Inhibition by Inorganic Dopants of γ-Alumina Chemical Weathering under Hydrothermal Conditions: Identification of Reactive Sites and their Influence in Fischer–Tropsch Synthesis, *ChemCatChem*, 2017, **9**(12), 2106–2117, DOI: 10.1002/cctc.201700140, (accessed 2025/11/09).
12 N. Fischer, B. Clapham, T. Feltes and M. Claeys, Cobalt-Based Fischer–Tropsch Activity and Selectivity as a Function of Crystallite Size and Water Partial Pressure, *ACS Catal.*, 2015, **5**(1), 113–121, DOI: 10.1021/cs500936t.
13 M. Claeys, M. E. Dry, E. van Steen, P. J. van Berge, S. Booyens, R. Crous, P. van Helden, J. Labuschagne, D. J. Moodley and A. M. Saib, Impact of Process Conditions on the Sintering Behavior of an Alumina-Supported Cobalt Fischer–Tropsch Catalyst Studied with an in Situ Magnetometer, *ACS Catal.*, 2014, **5**(2), 841–852, DOI: 10.1021/cs501810y, (accessed 7/27/2026).
14 J. Labuschagne, R. Meyer, Z. Chonco, J. Botha and D. Moodley, Application of water-tolerant Co/β-SiC catalysts in slurry phase Fischer–Tropsch synthesis, *Catal. Today*, 2016, **275**, 2–10.
15 D. J. Moodley, A. M. Saib, J. van de Loosdrecht, C. A. Welker-Nieuwoudt, B. H. Sigwebela and J. Niemantsverdriet, The impact of cobalt aluminate formation on the deactivation of cobalt-based Fischer–Tropsch synthesis catalysts, *Catal. Today*, 2011, **171**(1), 192–200.
16 J. van de Loosdrecht, I. M. Ciobîcă, P. Gibson, N. S. Govender, D. J. Moodley, A. M. Saib, C. J. Weststrate and J. W. Niemantsverdriet, Providing Fundamental and Applied Insights into Fischer–Tropsch Catalysis: Sasol–Eindhoven University of Technology Collaboration, *ACS Catal.*, 2016, **6**(6), 3840–3855, DOI: 10.1021/acscatal.6b00595, (accessed 10/12/2026).
17 E. Rytter and A. Holmen, Deactivation and regeneration of commercial type Fischer-Tropsch Co-catalysts—A mini-review, *Catalysts*, 2015, **5**(2), 478–499.
18 F. Diehl and A. Y. Khodakov, Promotion of cobalt Fischer-Tropsch catalysts with noble metals: a review, *Oil Gas Sci. Technol.*, 2009, **64**(1), 11–24.
19 A. M. Saib, J. L. Gauché, C. J. Weststrate, P. Gibson, J. H. Boshoff and D. J. Moodley, Fundamental Science of Cobalt Catalyst Oxidation and Reduction Applied to the Development of a Commercial Fischer–Tropsch Regeneration Process, *Ind. Eng. Chem. Res.*, 2014, **53**(5), 1816–1824, DOI: 10.1021/ie4027346, (accessed 10/12/2026).
20 A. De la Osa, A. De Lucas, J. Díaz-Maroto, A. Romero, J. Valverde and P. Sanchez, FTS fuels production over different Co/SiC catalysts, *Catal. Today*, 2012, **187**(1), 173–182.
21 A. Zimina, M. I. Fadlalla, J. Potgieter, C. E. Jimenez, R. Ilica, E. Sireci, D. I. Sharapa, D. de Oliveira, C. Hsu and E. Saraci, *et al.*, Comparison of Industrially Relevant Fischer–Tropsch Cobalt Catalysts Supported on Alumina and Modified Silica with Complementary In-Situ and Operando Characterization Methods, *J. Phys. Chem. C*, 2026, **130**(10), 3676–3690, DOI: 10.1021/acs.jpcc.5c05172, (accessed 10/12/2026).
22 P. Nguyen and C. Pham, Innovative porous SiC-based materials: From nanoscopic understandings to tunable carriers serving catalytic needs, *Appl. Catal., A*, 2011, **391**(1–2), 443–454.
23 S.-J. Park, J. W. Bae, G.-I. Jung, K.-S. Ha, K.-W. Jun, Y.-J. Lee and H.-G. Park, Crucial factors for catalyst aggregation and deactivation on Co/Al2O3 in a slurry-phase Fischer–Tropsch synthesis, *Appl. Catal., A*, 2012, **413–414**, 310–321, DOI: 10.1016/j.apcata.2011.11.022.
24 S.-J. Park, G. Kwak, Y.-J. Lee, K.-W. Jun and Y. T. Kim, Effect of H2O on Slurry-Phase Fischer–Tropsch Synthesis over Alumina-supported Cobalt Catalysts, *Bull. Korean Chem. Soc.*, 2018, **39**(4), 540–547, DOI: 10.1002/bkcs.11431.
25 R. M. Ravenelle, J. R. Copeland, W.-G. Kim, J. C. Crittenden and C. Sievers, Structural Changes of γ-Al2O3-Supported

 This journal is © The Royal Society of Chemistry 2026

Catalysts in Hot Liquid Water, *ACS Catal.*, 2011, **1**(5), 552–561, DOI: 10.1021/cs1001515.

26 SASOL, *S. P. C. Doped Aluminas*, SASOL, 2026, https://products.sasol.com/pic/products/home/grades/ZA/5puralox-and-siralox-doped/index.html, (accessed 12 January 2026).

27 M. Chaza, M. I. Fadlalla, T. M. Nyathi, N. Fischer and M. Claeys, Fischer-Tropsch synthesis over supported Ru catalysts for high syngas conversions: A comparative study of Al2O3 and SiOx-modified-Al2O3 supports, *Appl. Catal., A*, 2026, **711**, 120738, DOI: 10.1016/j.apcata.2025.120738.

28 E. P. Barrett, L. G. Joyner and P. P. Halenda, The determination of pore volume and area distributions in porous substances. I. Computations from nitrogen isotherms, *J. Am. Chem. Soc.*, 1951, **73**(1), 373–380.

29 K. N. M. F., *Soft X-Ray Spectroscopy, Microscopy, and Spectromicroscopy (WERA)*, KNMFi, 2024, https://www.knmf.kit.edu/WERA.php, (accessed 20 March 2026).

30 A. A. Coelho, Indexing of powder diffraction patterns by iterative use of singular value decomposition, *Appl. Crystallogr.*, 2003, **36**(1), 86–95.

31 *BWSpec Software*, Metrohm, https://www.metrohm.com/en_za/products/b/wt-8/bwt-810000044.html, (accessed 2026 10 October).

32 L. Fu, H. Yang, Y. Hu, D. Wu and A. Navrotsky, Tailoring mesoporous γ-Al2O3 properties by transition metal doping: a combined experimental and computational study, *Chem. Mater.*, 2017, **29**(3), 1338–1349.

33 E. J. Peterson, A. T. DeLaRiva, S. Lin, R. S. Johnson, H. Guo, J. T. Miller, J. Hun Kwak, C. H. F. Peden, B. Kiefer and L. F. Allard, *et al.*, Low-temperature carbon monoxide oxidation catalysed by regenerable atomically dispersed palladium on alumina, *Nat. Commun.*, 2014, **5**(1), 4885, DOI: 10.1038/ncomms5885.

34 J. Xue, D. Wang, M. Li and R. Jia, Preparation of silicon-modified gamma alumina coating through cathodic plasma electrolytic deposition, *Ceram. Int.*, 2019, **45**(15), 19345–19350.

35 E. López-Navarrete, A. Caballero, A. R. González-Elipe and M. Ocana, Chemical state and distribution of Mn ions in Mn-doped α-Al2O3 solid solutions prepared in the absence and the presence of fluxes, *J. Eur. Ceram. Soc.*, 2004, **24**(10–11), 3057–3062.

36 F. Liu, C. Okolie, R. M. Ravenelle, J. C. Crittenden, C. Sievers, P. C. A. Bruijnincx and B. M. Weckhuysen, Silica deposition as an approach for improving the hydrothermal stability of an alumina support during glycerol aqueous phase reforming, *Appl. Catal., A*, 2018, **551**, 13–22, DOI: 10.1016/j.apcata.2017.11.025.

37 P. Ildefonse, D. Cabaret, P. Sainctavit, G. Calas, A. M. Flank and P. Lagarde, Aluminium X-ray absorption Near Edge Structure in model compounds and Earth's surface minerals, *Phys. Chem. Miner.*, 1998, **25**(2), 112–121, DOI: 10.1007/s002690050093.

38 T. E. Westre, P. Kennepohl, J. G. DeWitt, B. Hedman, K. O. Hodgson and E. I. Solomon, A multiplet analysis of Fe K-edge 1s→ 3d pre-edge features of iron complexes, *J. Am. Chem. Soc.*, 1997, **119**(27), 6297–6314.

39 A. M. Saib, A. Borgna, J. van de Loosdrecht, P. J. van Berge and J. W. Niemantsverdriet, XANES study of the susceptibility of nano-sized cobalt crystallites to oxidation during realistic Fischer–Tropsch synthesis, *Appl. Catal., A*, 2006, **312**, 12–19, DOI: 10.1016/j.apcata.2006.06.009.

40 J. van de Loosdrecht, I. M. Ciobîcă, P. Gibson, N. S. Govender, D. J. Moodley, A. M. Saib, C. J. Weststrate and J. W. Niemantsverdriet, Providing Fundamental and Applied Insights into Fischer–Tropsch Catalysis: Sasol–Eindhoven University of Technology Collaboration, *ACS Catal.*, 2016, **6**(6), 3840–3855, DOI: 10.1021/acscatal.6b00595.

41 C.-T. Liu and W. T. Lindsay Jr., Vapor pressure of deuterated water from 106 to 300.deg, *J. Chem. Eng. Data*, 1970, **15**(4), 510–513, DOI: 10.1021/je60047a015.

42 F. Zheng, H. Zhu, T. Luo, H. Wang and H. Hou, Pure water leaching soluble manganese from electrolytic manganese residue: Leaching kinetics model analysis and characterization, *J. Environ. Chem. Eng.*, 2020, **8**(4), 103916, DOI: 10.1016/j.jece.2020.103916.

43 R. M. Mironenko, O. B. Belskaya, V. P. Talsi, T. I. Gulyaeva, M. O. Kazakov, A. I. Nizovskii, A. V. Kalinkin, V. I. Bukhtiyarov, A. V. Lavrenov and V. A. Likholobov, Effect of γ-Al2O3 hydrothermal treatment on the formation and properties of platinum sites in Pt/γ-Al2O3 catalysts, *Appl. Catal., A*, 2014, **469**, 472–482, DOI: 10.1016/j.apcata.2013.10.027.

44 T. He, L. Xiang and S. Zhu, Different nanostructures of boehmite fabricated by hydrothermal process: Effects of pH and anions, *CrystEngComm*, 2009, **11**(7), 1338–1342, DOI: 10.1039/b900447p.

45 X. Chen, H.-S. Huh and S. Lee, Hydrothermal synthesis of boehmite (γ-AlOOH) nanoplatelets and nanowires: pH-controlled morphologies, *Nanotechnology*, 2007, **18**, 285608, DOI: 10.1088/0957-4484/18/28/285608.